Received: 11 March 2021 | Revised: 26 October 2021 | Accepted: 28 October 2021

DOI: 10.1002/gdj3.137

Geoscience Data Journal | RMetS | WILEY

DATA PAPER

Hurricane Florence (2018): Long duration single- and dual-Doppler observations and wind retrievals during landfall

Michael I. Biggerstaff[1,2,3] | **A. Addison Alford**[2] | **Gordon D. Carrie**[1] | **Jeffrey A. Stevenson**[1]

[1]School of Meteorology, University of Oklahoma, Norman, Oklahoma, USA

[2]Cooperative Institute for Weather Research and Operations, University of Oklahoma, Norman, Oklahoma, USA

[3]Advanced Radar Research Center, University of Oklahoma, Norman, Oklahoma, USA

Correspondence
Michael I. Biggerstaff, 120 David L Boren Blvd Suite 5900, Norman, OK 73072, USA.
Email: drdoppler@ou.edu

Funding information
National Aeronautics and Space Administration, Grant/Award Number: 16-EARTH16F-0101, 17-EARTH17R-72 and 18-EARTH18R-0086; National Science Foundation, Grant/Award Number: RAPID AGS-1902593; National Institute for Standards and Technology, Grant/Award Number: 70NANB19H056; University of Oklahoma

Abstract

A ground-based C-band Shared Mobile Atmospheric Research and Teaching (SMART) polarimetric radar and the National Weather Service WSR-88D radar near Wilmington, North Carolina simultaneously observed Hurricane Florence (2018) as it made landfall as a category 1 hurricane. The slow translation of Florence allowed for more than 30 hr of data collection before, during and after the tropical cyclone came ashore. Nearly 26 hr of three-dimensional wind retrievals every 6–10 min were constructed from the radar observations, providing an unprecedented view of the evolution of rainbands, the inner core and the eyewall of Hurricane Florence. This article describes the radar data, the procedures used for automated quality control, data processing and the wind retrievals that have been constructed. The location of the data and wind retrieval archive is given. These data can be used to study the dynamics and rainfall of Hurricane Florence, to quantify the impact of winds on the natural and built environment, to validate numerical simulations of the tropical cyclone, and as an educational resource for courses in radar and tropical meteorology.

KEYWORDS

Florence (2018), hurricane, landfalling tropical cyclone, SMART radar

Dataset

Identifier: https://doi.org/10.5281/zenodo.4594350

Creators: M. I. Biggerstaff, A. A. Alford, J. A. Stevenson, and G. D. Carrie

Title: SMART radar and KLTX WSR-88D data and wind retrievals during the landfall of Hurricane Florence (2018)

Publisher: Zenodo Archive

Publication year: 2021

Resource type: Dataset

Version: 2

1 | INTRODUCTION

Hurricane Florence (2018) was a long-lived tropical cyclone (TC) that underwent two cycles of rapid intensity changes before making landfall near Wrightsville Beach, North Carolina on 14 September as a high-end category 1 hurricane (Stewart & Berg, 2019). As part of the hurricane-at-landfall research programme at the University of Oklahoma (OU), a C-band (5.37-cm wavelength) Shared Mobile Atmospheric Research and Teaching (SMART) radar (Biggerstaff et al., 2005) was deployed near Wilmington, NC to intercept Florence during landfall (Figure 1). The rural area in that part of North Carolina is heavily wooded with pine trees that reach up to 30 m in height. Fortunately, a bridge on Interstate Highway 140 over the Cape Fear River was recently built 25 m above the river with an extra wide shoulder, providing an excellent location and mostly open view for the truck-based SMART radar.

Steering currents for Florence were weak during landfall, and the hurricane translated slowly (~8 m/s), which resulted in heavy flooding in North and South Carolina. The slow forward speed of Florence afforded an unprecedented opportunity for an exceptionally long observing period. More than 30 hr of data were collected with the SMART radar. When combined with the National Weather Service (NWS) Weather Surveillance Radar—1988 Doppler (WSR-88D; Crum & Alberty, 1993) supporting the Wilmington, NC Weather Service Office (KLTX), about 26 hr of three-dimensional wind retrievals throughout the hurricane were able to be constructed. This is the longest record to date of wind retrievals from a dual-Doppler network that has ever been produced for a landfalling tropical cyclone.

Past wind retrievals using the SMART radars have elucidated the structure and evolution of supercell thunderstorms (Bela et al., 2018; Betten et al., 2018; Calhoun et al., 2013; Davenport et al., 2019; DiGangi et al., 2016; Fried et al., 2016; Huntrieser et al., 2016; Li et al., 2017; Skinner et al., 2011) and mesoscale convective systems (Barth et al., 2015; Geerts et al., 2017; Lund et al., 2009; Miller et al., 2020; Palucki et al., 2011). The relationship between radar observed kinematics and cloud electrification for both natural lightning (Biggerstaff et al., 2017; Bruning et al., 2010; Chmielewski et al., 2020; Kuhlman et al., 2009; MacGorman et al., 2008; Payne et al., 2010) and triggered lightning (Hare et al., 2016; Hill et al., 2013; MacGorman et al., 2015; Pilkey et al., 2013) has also been studied with SMART radar observations. Additionally, the boundary layer structure of landfalling TCs has been documented using SMART radars (Alford et al., 2020; Hirth et al., 2012; Knupp et al., 2006; Lorsolo et al., 2008), as has the existence of mesovortices along the inner edge of hurricane eyewalls (Alford et al., 2019b; Fernandez-Caban et al., 2019). Alford et al. (2019b) mapped the maximum winds observed during the landfall of major hurricane Harvey (2017) and found that the storm was a category 3, rather than the current official rating of category 4, hurricane at the time of landfall.

Herein we describe the SMART radar observations, data processing and the associated wind retrievals obtained from the Hurricane Florence deployment. This article is structured as follows: Section 2 describes the deployment of the SMART radar and the radar tasks prescribed to collect dual-polarization and radial velocity data. A brief description of the WSR-88D data is also provided. Section 3 summarizes the quality-control steps taken to produce research-ready radial velocity observations to use in dual-Doppler analysis. Section 4 describes processes taken to retrieve dual-Doppler-derived winds from the SMART radar and KLTX. Section 5 documents the location and format of the dataset. Section 6 concludes

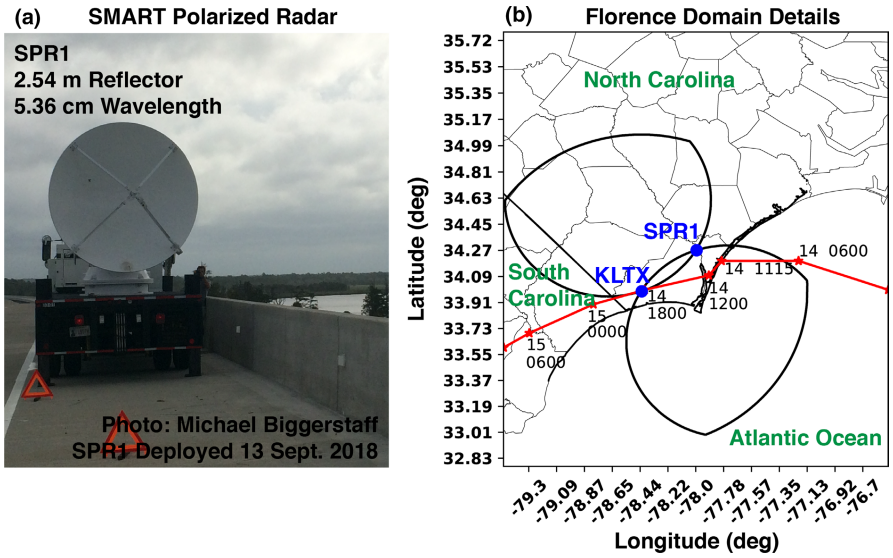

FIGURE 1 (a) Photo of SMART polarimetric radar unit 1 (SR1-P) deployed on the L. Bobby Brown Bridge on Interstate 140 over the Cape Fear River at 34.273021°N, 78.001625°W. (b) Details of the dual-Doppler domain. The 20° cross-beam angles of the western and eastern lobes are contoured in black. The SMART polarimetric radar and the NWS KLTX positions are denoted by the blue markers. The red line indicates the Best Track positions of Hurricane Florence in 6-hr intervals. The 6-hr UTC intervals are indicated by the stars with time labels

the work by commenting on the data significance and potential use.

2 | DATA COLLECTION

The spatially contiguous broad-area precipitation in TCs can severely limit centimetre wavelength radar observations due to the attenuation of the radar signal (Doviak & Zrnić, 1993). Luckily, for this dataset, the contributing radars operate at C- and S-band, and attenuation loss was minimal. Hence, the spatial extent of the analyses was mostly limited by the operational range of the radar systems.

2.1 | SMART radar data

The SMART radar that deployed for Hurricane Florence had just been rebuilt and upgraded to dual-polarization diversity. While the truck platform remained the same as described in Biggerstaff et al. (2005), many of the radar characteristics changed. Table 1 lists the specifications of the new SMART polarimetric radar unit 1, or SR1-P, which was previously referred to as SR1 before the dual-polarization upgrade. The radar was located on the shoulder of the Interstate-140 L. Bobby Brown bridge over the Cape Fear River to the north-west of the city of Wilmington, NC. The site (34.273021°N, 78.001625°W) was 20 km inland from the Atlantic Ocean coastline. The NWS WSR-88D KLTX radar is located about 50 km south-west of the city of Wilmington at 33.989147°N and 78.429108°W. The baseline connecting the two radars was 50.5 km with KLTX oriented at an azimuth angle of 231.4° from north relative to SR1-P. The SR1-P radar was levelled using hydraulic outriggers and a digital leveller mounted in the base of the pedestal with a display in the truck cab. The radar remained level throughout the deployment as verified by the in-cab display.

SR1-P operated in simultaneous transmit and receive (STaR) mode (Doviak et al., 2000) to collect dual-polarization data along with radial velocity. The SMART radars have a half-power beamwidth of approximately 1.5°, but data are oversampled to an effective resolution of 1° in azimuth. Operations in Florence began at 1306 UTC on 13 September 2018 and concluded with the last volume scan at 1943 UTC on 14 September. Due to the receiver losing track of the burst pulse from the transmitter, the radar was inoperable for a 96-min period from 1846 to 2022 UTC on the 13th. Shorter periods of downtime occurred from 0549 to 0600 UTC, 1106 to 1120 UTC, and from 1132 to 1148 UTC on the 14th either due to changes in scanning strategy or power disruptions in the azimuthal antenna drive.

After documenting the clutter from buildings and trees (mostly between 90° and 100° in azimuth) at the beginning of the observational period, SR1-P conducted continuous low-level surveillance scans from 1322 to 1343 UTC. Each scan took about 21 s to complete. This allowed the operator time to program the other tasks used during the deployment. Those tasks were tested before finalizing the scanning strategy. Starting at 1424 UTC on the 13th, the radar began a well-defined 12-min cycle of tasks. The first minute was dedicated to a low-level surveillance scan. That scan was followed by three, volumetric, plan position indicator (PPI) sector scans covering the eastern dual-Doppler lobe (Figure 1b) over a 10-min period. The final minute in the cycle was used to perform a user-specified range height indicator (RHI) scan through a feature of interest or along the azimuth where a disdrometer had been placed to measure the raindrop size distribution. With time, the hurricane's outer rainbands moved over the western dual-Doppler lobe. At 2300 UTC on the 13th, the three eastern sector volume scans were replaced with two full 360° plan position indicator (PPI) volume scans, so winds could be retrieved in both dual-Doppler lobes. The radar remained in that mode of operation until the end of the observing period. Table 2 lists the characteristics of the various tasks that were used.

The precipitation structure sampled by SR1-P varied as the hurricane washed ashore. Initially, only outer rainbands were in the eastern dual-Doppler lobe. The eyewall and inner core radar reflectivity were highly asymmetric with the precipitation-free side closest to the radar domain. The eyewall precipitation rotated quickly around the centre of circulation such that by 04 UTC on the 14th, it was approaching the radars. Both outer rainbands and the inner core were being well sampled by 06 UTC. Two hours later, the western portion of the eyewall had increased in precipitation coverage such that winds in that part of the storm were able to be retrieved in the eastern dual-Doppler lobe. Luckily, this part of the eyewall had the strongest radar returns as the centre of circulation approached the coast. The eyewall was over SR1-P by 10 UTC on the 14th and remained so for 2.5 hr as the eye contracted in size within the eastern dual-Doppler lobe. This dataset may be the best example of eyewall contraction during landfall that has been collected to date. The eye was completely filled with precipitation by 15 UTC as the centre of circulation approached the baseline connecting the two radars, where winds cannot be retrieved. SR1-P continued to sample the remnant eyewall and inner core precipitation for the next few hours as the main precipitation moved over the western dual-Doppler lobe. However, the rain-free portion of the inner core travelled over the domain by

TABLE 1 Specifications of polarimetric diversity upgraded SMART radar unit 1 (SR1-P)

Transmitter
300 kW magnetron; 0.001 duty cycle; frequency is 5589 MHz.
Pulse durations of 0.25, 0.5, 1.0 or 2.0 μs (selectable)
Simultaneous transmit and receive dual-polarization (150 kW in each channel)
Can also operate in H transmit and H/V receive to measure linear depolarization ratio
Antenna
2.4 m solid parabolic reflector; 1.5° half-power circular beam width
Gain: ~40 dB; first sidelobe: −26 dB down (one way)
Minimum detectable signal: −108 dBm
Pedestal
Refurbished SCR-584 with up to 36° s^{-1} rotation in azimuth and 12° s^{-1} in elevation
0° to 90° elevation limits
Signal processor
SIGMET/Vaisala RVP-9
Time series I&Q capable
Dual-pol or H only processing
Pulse pair, fast Fourier transform, dual-PRF, staggered PRT or random phase signal processing
Radial resolution, dependent on pulse duration, down to 33 m
Nine levels of clutter filtering possible; data can be threshold on signal quality parameters
Full PPI, sector scan PPI, RHI or pointing mode capable
Output moments are radar reflectivity (filtered and unfiltered), signal quality index, radial velocity, spectrum width, differential radar reflectivity, differential phase, specific differential phase, co-polar correlation coefficient, linear depolarization ratio (H-only transmit mode), cross-pol correlation coefficient (H-only transmit mode)
A-scope, RHI and PPI real-time displays
Base products can be generated for animation or inspection of any output moment
Data recorded in native IRIS format raw volumes
Platform
International Truck model 4700 dual, extended cab.
Length: 10.1 m (33 ft); height: 4.1 m (13 ft 6 in.); weight 11,567 kg (25,500 lb)
Four hydraulic outriggers for leveling; 10 kW diesel generator for power to radar
190 L (50 gallon) dedicated tank for generator; two 190 L (50 gallon) tanks for truck engine

18 UTC, minimizing the area where winds could be retrieved. Eventually operations were terminated due to crew fatigue and the lack of precipitation in the analysis domain.

2.2 | WSR-88D radar data

The NWS WSR-88D radar serving Wilmington, NC (KLTX) switched from operating in volume coverage pattern (VCP) 215 to VCP 212 at 0822 UTC on 13 September 2018. With the exception of 1934–1948 UTC on 13 September when the radar was operated in VCP 12, the KLTX radar remained in VCP 212 mode throughout the landfall of Florence. All three VCPs have elevation angle sequences that start at 0.5° and end at 19.5°, with oversampling of the atmosphere at the lower levels. The primary difference is that VCP 215 takes data at 15 unique elevation angles over a 6-min period of time, while VCPs 12 and 212 take data at 14 unique elevation angles over approximately 4.5 min. The only difference between VCPs 12 and 212 is that VCP 212 makes use of the SZ-2 phase encoding technique (Zittel et al., 2008) to mitigate range folding.

Only data from VCPs 12 and 212 were included in the dual-Doppler analyses documented here. The VCP 12 and 212 elevation sequence is 0.5°, 0.9°, 1.3°, 1.8°, 2.4°, 3.1°, 4.0°, 5.1°, 6.4°, 8.0°, 10.0°, 12.5°, 15.6° and 19.5°. At the discretion of the radar operator, the WSR-88D can repeat the lowest sweep mid-way through the volume time, which is typically after the 3.1° elevation sweep. While the WSR-88D radars are 1° circular beamwidth radars, the data are oversampled in azimuth and recorded every 0.5° in azimuth. The range resolution is 250 m for all variables.

3 | DATA QUALITY CONTROL

The data quality control procedures used here were similar to those used for the Harvey dataset documented in Alford et al. (2019a) with a few modifications described below. As such, all 30 hr of PPI volumetric SMART radar data collected during Hurricane Florence have been preliminarily quality controlled. Since the goal of our research is to develop maps of the wind characteristics during landfalling hurricanes and to understand the circulations that produce significant wind damage, the quality control focused on the radial velocity field. No attempt was made to correct the radar reflectivity for attenuation or to verify or edit the dual-polarimetric variables. An RHI scan taken through the eyewall at 1023 UTC on the 14 September (Figure 2) illustrates the inherent quality of those fields as well as the raw radial Doppler velocity. As demonstrated in Figure 2f, we recommend utilizing surveillance sweep data to place RHI data in context due to their close temporal proximity.

The effect of modest attenuation in radar reflectivity is evident in the RHI scan through the eyewall

TABLE 2 Details of SMART radar (SR1-P) tasks during the landfall of Hurricane Florence

Task name	Azimuthal coverage	Time in 12-min cycle	Hours performed	Elevation angles (°)	PRF (Hz)/ Nyquist (m/s)	Moments
WINDS, WINDS2	360°	2–6, 7–11	1404 to 1413 UTC 13 Sept. 2206 UTC 13 Sept. to 1943 UTC 14 Sept.	0.8, 1.5. 2.3, 3.2, 4.0, 4.7, 5.5, 6.2, 7.0, 8.0, 9.0, 10.0, 11.0, 12.0, 14.0, 16.0, 18.0, 20.0, 23.0, 26.0, 29.0	1200/16.0	Z_H, V_R, W, SQI, Z_{DR}, Φ_{DP}, K_{DP}, ρ_{HV}
RHI	Varying according to operator	12	1346 UTC 13 Sept. to 1132 UTC 14 Sept.	2–45	900/12.0	Z_H, V_R, W, SQI, Z_{DR}, Φ_{DP}, K_{DP}, ρ_{HV}
E1, E2, E3	150°	2–4, 5–7, 8–10	1349 UTC to 2204 UTC 13 Sept.	0.8, 1.5, 2.3, 3.2, 4.0, 4.7, 5.5, 6.2, 7.0, 8.0, 9.0, 10.0, 11.0, 12.0, 14.0, 16.0, 18.0, 20.0, 23.0, 26.0, 29.0	1200/16.0	Z_H, V_R, Z_{DR}, Φ_{DP}, ρ_{HV}
SURV	360°	1	1322 to 1343 UTC 13 Sept., continuously 1348 UTC 13 Sept. to 1936 UTC 14 Sept.	1.0, 1.5 or 1.5 only	750/10.0	Z_H, V_R, W, SQI, Z_{DR}, Φ_{DP}, K_{DP}, ρ_{HV}
CLTR	360°	N/A	1306–1320 UTC 13 Sept.	0.8, 1.5, 2.3, 3.1, 3.8, 4.5, 5.2, 5.9	950/12.7	Z_H, V_R, W, SQI, Z_{DR}, Φ_{DP}, K_{DP}, ρ_{HV}

(Figure 2a) as the precipitation intensity in the outer eyewall (beyond 35 km range) is notably less than that observed in the portion closer to the radar (within 20 km range). Nevertheless, the impact of the vertical wind shear felt by the hurricane is evident as the westward slope of the eyewall with height is easily discernible. The enhanced differential radar reflectivity associated with the melting band is observed at an altitude of about 5.5 km (Figure 2b). Particularly oblate targets were apparently also present below 2 km altitude from 5 to 8 km range from the radar where differential radar reflectivity was again enhanced. This low-level feature was also associated with high values of specific differential phase (Figure 2e), which, at these altitudes, indicates a region of particularly heavy rainfall. Another area of heavy rain was observed between 10 and 15 km range. Both the melting level and the low-level enhanced differential radar reflectivity area were associated with low correlation coefficients (Figure 2c). Mixed phased precipitation associated with the melting of snow and graupel in the

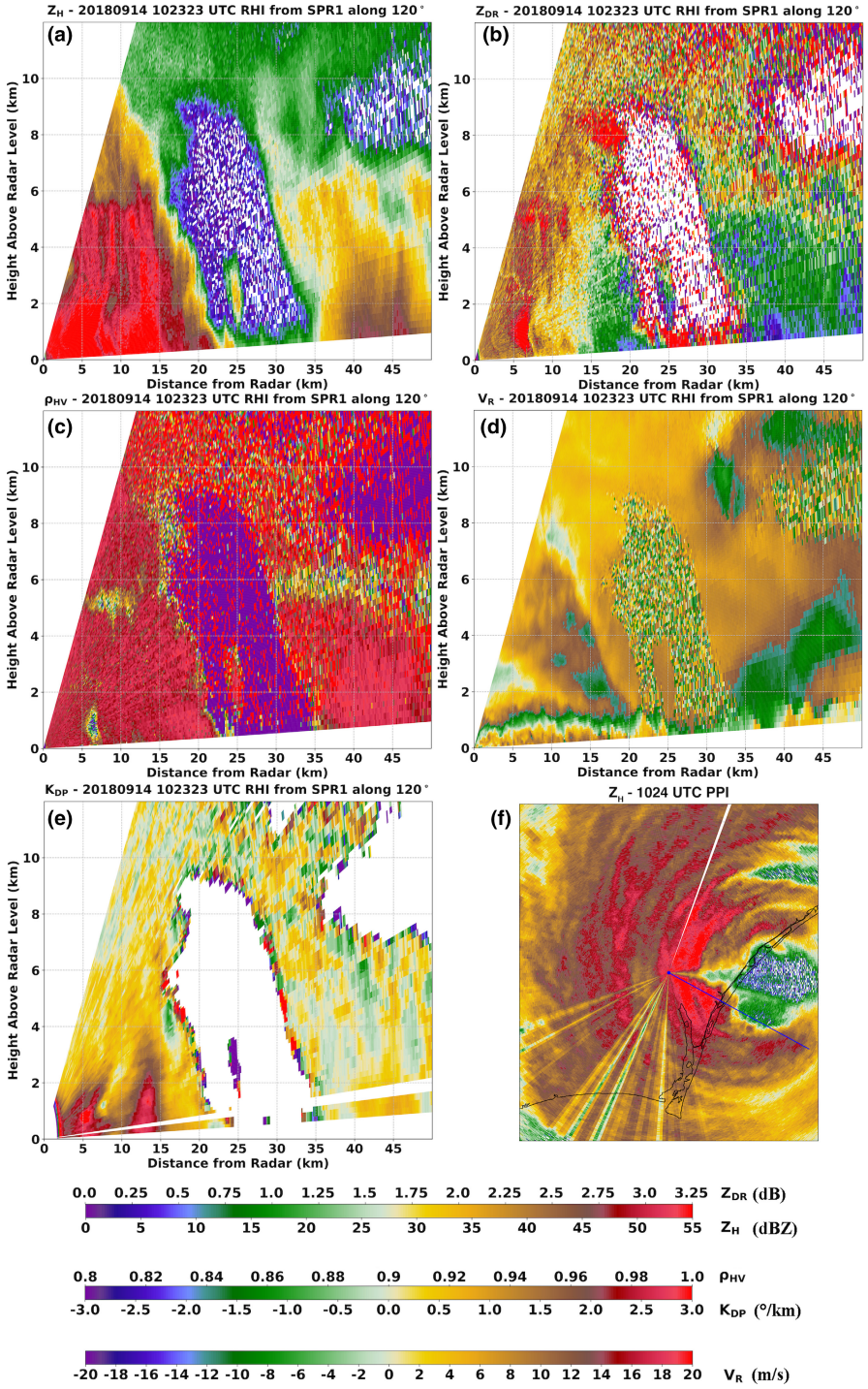

FIGURE 2 Illustration of raw data quality using (a)–(e) Range Height Indicator and (f) Plan Position Indicator scans through the eyewall and eye of Hurricane Florence at 1023 and 1024 UTC, respectively, on 14 September 2018: (a) radar reflectivity (Z_H), (b) differential radar reflectivity (Z_{DR}), (c) correlation coefficient (ρ_{HV}), (d) radial velocity (V_R) and (e) specific differential phase (K_{DP}). The values for each variable are in the units given on the associated colour bars. The location of the RHI relative to the low-level radar reflectivity structure is shown in (f), which is a 1.5° elevation angle PPI scan of radar reflectivity. Note that the range of the RHI scans extends out farther than indicated in the figure

melting level is known to result in low correlation coefficient (Matrosov et al., 2007). While it is possible that the lower altitude area of low correlation coefficient was associated with either biological targets (Stepanian et al., 2016) or debris (Ryzhkov et al., 2005) that had been lofted by the hurricane circulation, it is more likely that Mie scattering by precipitation sized droplets beyond 5 cm in diameter effectively reduced the correlation coefficient magnitude (e.g., Zrnić et al., 2000).

The noisy regions in the raw radial velocity field (Figure 2d) indicate that the attenuated minimum detectable signal was about 3 dBZ at 25 km range. The apparent discontinuity in velocity values around 12 m/s marks the Nyquist velocity (12.06 m/s) for the RHI scans. The velocity field is smooth and, once noise is removed, can be easily dealiazed by an automated dealiasing algorithm. However, the data processing reported here was not applied to the RHI or surveillance PPI data. Regardless, the structure of the flow is well defined, including the small-scale boundary layer (below ~2 km altitude) turbulent features often noted in hurricanes (Foster, 2005) that have been linked to increased potential for damage (Morrison et al., 2005).

To conduct the automated dealiazing needed for the wind retrievals, the volumetric PPI radial velocity data were first run through several preprocessing steps using the authors' own software. Raw Doppler velocity (see Figure 3a) gates characterized by low (<0.07) Signal Quality Index (SQI) were removed. SQI is a variable calculated by Sigmet/Vaisala signal processors to determine the quality of data in each radar range gate (Vaisala, 2014). It is a function of both signal-to-noise and spectrum width and represents the autocorrelation at lag 1 of the clutter-filtered time series of the complex voltage and its conjugate measured by the radar. The value varies from 0 for white noise to 1 for pure tone. The SQI field is included in the radar data archive. While values of SQI higher than the selected threshold can still represent gates with low signal-to-noise (SNR) ratio, we begin the objective process of removing gates at very low values to retain as much information as possible. Next, a rolling, 20-gate standard deviation of Doppler velocity at each gate was calculated in radius and azimuth independently. The minimum between the two rolling standard deviations for any gate whose radar reflectivity was below 5 dBZ was assigned as a 'final' standard deviation to each gate. If the gate's 'final' standard deviation exceeded 16 m/s, it was removed. Effectively, this removed all noise in the Doppler velocity field in regions of low SNR. A despeckling function over a width of five gates was finally employed to remove any speckled gates remaining in low SNR regions. A speckled gate is one with a velocity value significantly different from the velocity values at neighbouring gates.

The Python ARM Radar Toolkit (Py-ART; Helmus & Collis, 2016) software package was used to objectively dealiase the Doppler velocity data for all sector and 360° volumes, excluding RHI and surveillance volumes. The region-based method in Py-ART was employed to objectively process all data collected between 1424 UTC on 13 September and 1943 UTC on 14 September. For Hurricane Harvey, Alford et al. (2019a) used two methods, the region-based method and the four-dimensional method (James & Houze, 2001), for dealiazing due to the extreme shear of the horizontal wind in Hurricane Harvey. Using the region-based method in Harvey, the horizontal wind shear tended to result in a greater number of errors resulting in Doppler velocities being dealiazed into the wrong interval. However, in Florence, the region-based method was largely successful. The few errors produced by the region-based method were further quality controlled subjectively using the National Center for Atmospheric Research Solo3 software package (Oye et al., 1995) to produce a final quality controlled version of the data (see Figure 3b). To increase productivity, some erroneous gates outside of the dual-Doppler domain may have been retained. The final products should be examined prior to use.

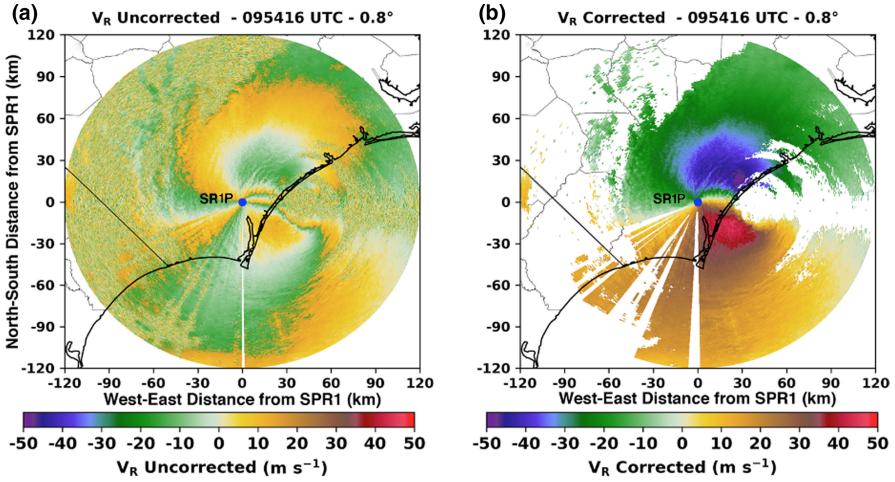

FIGURE 3 An example of the dealiazing by the objective and subjective methods employed in this dataset. (a) Aliased Doppler velocities (m/s) are shown from SR1-P at 0954:16 UTC for the 0.8° elevation PPI. (b) Dealiazed Doppler velocities from (a) are displayed

KLTX data in Level II format were retrieved from the National Centers for Environmental Information (NCEI; available online at https://www.ncdc.noaa.gov/data-access/radar-data) and were processed in a similar fashion. SQI values were not available for WSR-88D data for use in the initial threshold step. Instead, radial velocity data were excluded if the gate's reflectivity was characterized by values <0 dBZ. The data were then passed through the same standard deviation filter as above before Py-ART's region-based dealiazing scheme was applied to correct the aliased Doppler velocities for the entire dataset. The region-based method, as with SR1-P, was sufficient and produced minimal velocities dealiazed into the incorrect interval. The data are also included for reference in the Zenodo archive. While the automatically dealiazed data were examined manually using Solo3, very few subjective edits were needed.

4 | DUAL-DOPPLER ANALYSIS

Dual- and multiple-Doppler analysis is often used to retrieve the three-dimensional flow within storms and to characterize the spatial and temporal evolution of convective systems. Errors common to dual-Doppler analyses are often related to the temporal and spatial offset of radar observations, the underlying assumptions of mass continuity and the under-sampling of the boundary layer or storm top divergence (Chong et al., 1983; Dowell & Shapiro, 2003; Potvin et al., 2012b; Shapiro et al., 2010).

The SMART radar and KLTX were operated in a quasi-time synchronous task cycle to reduce the spatial offset of observations. After discussion with the National Weather Service in Wilmington, the task cycle described in Section 1 was chosen to collect SMART radar data as close as possible to KLTX data collection. The radar with the least numerous total volumes (KLTX) was identified to account for the maximum number of dual-Doppler analyses possible. For each KLTX volume, the central (mean) volume time was used to select the SMART radar volume whose central volume time was the nearest to KLTX's for dual-Doppler analysis. Figure 4 shows the difference in the central volume time between the volume pairs used in the dual-Doppler wind retrievals. Most pairs were offset by <2.5 min.

4.1 | Natural neighbour interpolation

The processed volumes were passed into a natural neighbour (Sibson, 1981) scheme modified from Betten et al. (2018) to interpolate each radar volume to a common Cartesian grid of 1 km horizontal and 0.5 km vertical resolution. The advantage of natural neighbour interpolation compared with other common interpolation methods (e.g., Barnes, 1994 or Cressman, 1959) is that the inherent resolvable scale of the radar data is somewhat preserved. Hence, grid locations close to the radar will retain observed small-scale variability, while grid locations at farther ranges from the radar will retain variability at the scale of the spatial distance between neighbouring azimuth and elevation angles.

To preserve the shape of the dealiazed and noise-threshold data volume, the natural neighbour scheme is applied in a series of two-dimensional steps. First, each PPI of Doppler velocity and radar reflectivity (converted to a linear scale) is interpolated to a regular azimuthal grid with 1° spacing. This azimuthal interpolation is performed to reconstruct RHIs from the PPI data at each azimuth and is necessary because the recorded azimuths of the raw PPI data can vary on the order of tenths of a degree between elevation tilts. Note that the reflectivity data volume may have a slightly different shape than the Doppler velocity data volume due to the removal of noisy velocities. Masks of both of these arrays (defined as 1 where data exist and 0 where data are removed) are also azimuthally interpolated. To later aid the dual-Doppler analysis, a two-dimensional Gaussian filter is applied to the interpolated Doppler velocity mask with a sigma of 4. Interpolated Doppler velocity and reflectivity are removed where their interpolated mask values are <0.4.

A second two-dimensional natural neighbour interpolation is then performed to create a common range–height grid for each regularly spaced azimuth of reflectivity, Doppler velocity and their masks. The range grid has 100-m resolution and extends from the first gate to the last gate of the radar PPI. The height grid is defined according to the grid specifications that will be used in the dual-Doppler wind retrievals. At this point, some extrapolation vertically (no more than one grid level or 500-m distance for this case) is allowed by retaining the Doppler velocities such that the Doppler velocity mask is above 0.4. Given the lowest analysis level of this dataset is at 500 m altitude, the downward extrapolation mainly affects grid points beyond ~80 km from the radars where the curvature of the Earth and vertical profile of the index of refraction combine to result in the lowest elevation angle (0.8°) being above the lowest analysis level (500 m). This procedure slightly expands the contiguous data available at the lowest analysis level, which is useful in applying the mass continuity constraint in the dual-Doppler wind retrieval described below. This technique is similar to other dual-Doppler radar studies using weighting function-based interpolation. All reflectivity data with a mask greater than 0 are retained.

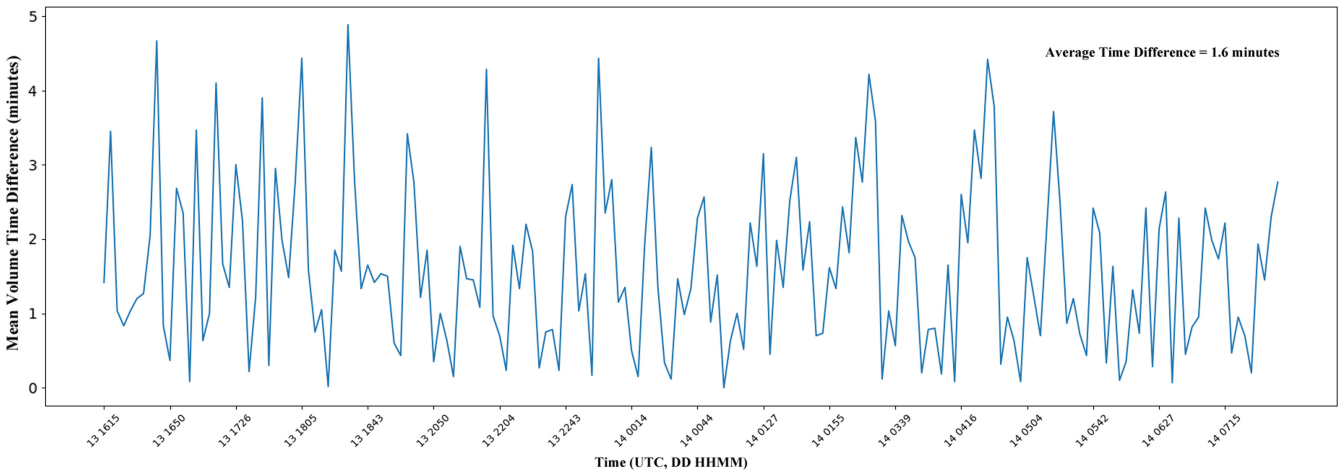

FIGURE 4 Time series of the difference in the mean volume times (in minutes) used in the dual-Doppler wind retrievals. Note that the time scale on the horizontal axis is in the day (13th or 14th of September 2018) followed by the UTC hour and minute

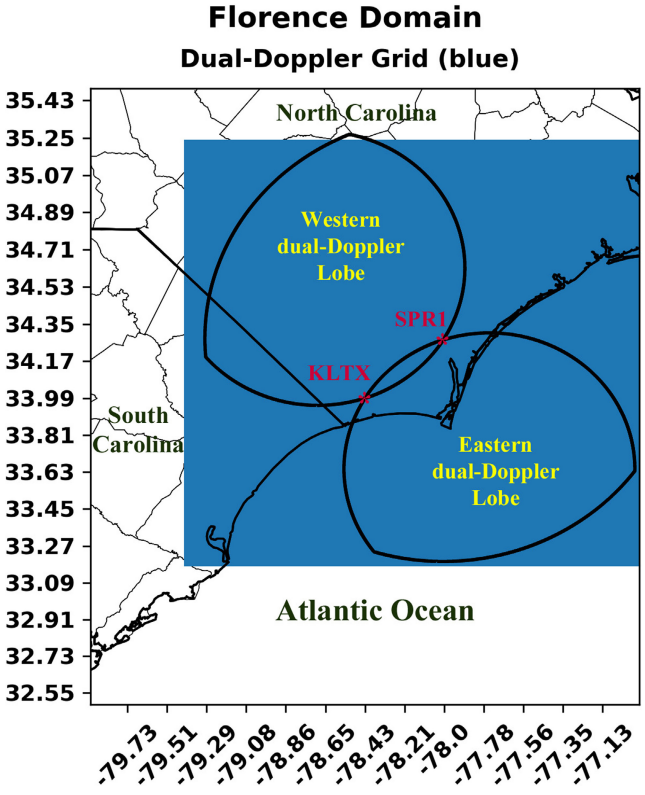

FIGURE 5 Dual-Doppler grid (blue box) relative to the areas in which the three-dimensional winds can be retrieved in the western and eastern dual-Doppler lobes (black outlined areas). The radar locations are denoted by the red stars. The vertical axis is latitude in degrees north. The horizontal axis is longitude in degrees east

The result of the first two interpolation steps is a three-dimensional volume of data defined in a cylindrical coordinate system. The final natural neighbour interpolation takes each height level in the cylindrical coordinate system and interpolates the data onto a Cartesian grid with the spacing and size defined by the dual-Doppler wind retrieval requirements. Additional data smoothing is applied in the Cartesian domain to aid the smoothness constraint embedded in the dual-Doppler 3D Var wind retrieval method. The Cartesian interpolated Doppler velocity mask, reflectivity mask and Doppler velocities at each height are passed through a Gaussian filter with a sigma of 1. Finally, the interpolated masks are applied to retain Doppler velocity and reflectivity data where their respective masks have values above 0.2. This threshold allows some extrapolation of the data volume horizontally (no more than one grid cell or 1 km in this case), which is helpful when computing the divergence field using finite differencing during the dual-Doppler wind retrievals.

4.2 | Dual-Doppler details

The origin of the dual-Doppler grid created here is located at KLTX at 0 km above mean sea level. The minimum x, y and z locations of the grid were set to −90, −90 and 0.5 km, respectively. The grid spans 230, 230, by 20 grid points in the x, y and z directions, respectively, with increments of 1 km horizontally and 0.5 km vertically. Figure 5 shows the analysis grid relative to the dual-Doppler lobes on each side of the radar baseline. The Cartesian wind retrieval domain was chosen to include both quasi-elliptical dual-Doppler lobes. As such, there are areas within the analysis domain in which no retrieved winds were possible due to beam geometry not providing linearly independent measurements.

The temporal offset between radar volumes from KLTX and the SMART radar was limited to 5 min maximum but was generally on the order of 2–3 min. As the intent of

the data collection was focused on mesoscale processes, the spatial/temporal offset of sub-kilometre scale features should induce minimal error as argued in Alford et al. (2019a). The curvature of the horizontal wind made typical linear-velocity advection correction (e.g., Ziegler, 2013) impossible. In the future, we intend to test recently developed techniques using objective non-linear advection correction schemes (e.g., Shapiro et al., 2021). But that advection correction method has not yet been applied to the data.

The Cartesian radar volumes were passed into a three-dimensional variational dual-Doppler wind retrieval algorithm documented in Potvin et al. (2012a). The procedure, as applied here, minimizes a total cost function composed of two separate constraining cost functions associated with the radial velocity measurement and mass continuity. The radial velocities were corrected for the influence of terminal velocity of the hydrometeors using density-weighted power-law fall speed-reflectivity relationships for rain and snow separately following Biggerstaff and Houze (1991). As in Alford et al. (2019a), the smoothness constraint in Potvin et al. was replaced with a one-step Leise filter (Leise, 1981) applied on the retrieved wind components every 50 iterations of the cost function and is similar to the technique inherent to Jackson et al. (2020). The variational technique is advantageous over traditional techniques, since the explicit integration (and associated errors) of the mass continuity equation is not employed. The cost function was minimized as described in Potvin et al.

The retrieved winds at 0.5 km above mean sea level at the time of the landfall of Hurricane Florence (1256 UTC on 14 September 2018) demonstrates the dual-Doppler analysis procedure (Figure 6). The maximum reflectivity between the two contributing radars and the horizontal wind vectors are shown in Figure 6a. The asymmetric nature of Florence was evident in the reflectivity field with the strongest part of the eyewall approaching the baseline between the radars, where winds cannot be retrieved. At this time, some of the fastest winds (45–50 m/s) were actually observed in the outer rainband across the western dual-Doppler lobe (Figure 6b). Pockets of winds with similar strength were also observed in the eastern eyewall. But the eyewall winds, in general, had already been diminished by increased friction over land and the overall weakening of the primary vortex circulation prior to landfall.

5 | ARCHIVE INFORMATION AND DATA FORMAT

5.1 | PPI and RHI data

All SMART radar and KLTX data are stored at the Zenodo archive with https://doi.org/10.5281/zenodo.4594350. The data are separated by radar. The SR1-P dataset is partitioned into RHI, full 360° PPI volumes, sector PPIs and surveillance scans. KLTX did not collect surveillance or RHI data. The edited volumes contain both the raw and dealiazed velocity fields. The radar data are presented in cfradial netCDF format (Dixon, 2010). This data format is easily malleable by common software packages used in radar processing (e.g., Py-ART or RadxConvert). Included in each subset directory is a file detailing the header information present in the netCDF files.

The raw SR1-P data also exist at https://doi.org/10.5281/zenodo.4592632 in native format with a reference to documentation on how to read the IRIS_DATA files.

5.2 | Dual-Doppler data

The dual-Doppler dataset is also contained in the Zenodo archive. The files are archived in netCDF format (Rew

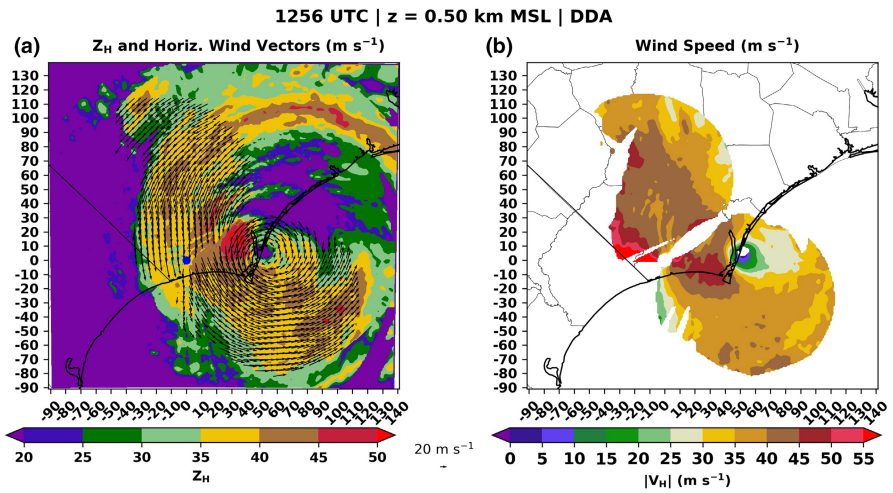

FIGURE 6 An example of a dual-Doppler analysis at 14 September 2018 1256 UTC at 0.5 km above mean sea level. (a) Reflectivity (colour-filled contours according to the colour bar) is shown with horizontal wind vectors overtop the reflectivity. (b) The magnitude of the horizontal wind speed is displayed according to the colour bar

et al., 2018). Each dual-Doppler analysis is denoted by the average times of the two contributing radar volumes. Within each file, a maximum reflectivity field is included, which is simply the maximum of the 1-km interpolated reflectivity values at each grid point between the two contributing radar volumes. Kinematic fields include u (east-west), v (north-south) and w (vertical) wind components. In addition, a coverage variable is also included. The coverage value of 1 indicates that a grid point within the dual-Doppler lobe contains data. A value of 0 indicates that the point is either outside of the area in which the two radar beams intersect at an angle >20° (i.e., the dual-Doppler lobe) or contains no data. Similar to the raw and dealiazed radar data, a file detailing the netCDF file header information is included in the archive.

6 | SIGNIFICANCE AND USE OF DATA

The dataset presented herein affords the opportunity for extensive analysis of Hurricane Florence's wind and precipitation fields prior to, during and after landfall. Using C- and S-band radar data with little attenuation due to precipitation provides mesoscale retrievals of winds and dual-polarization observations during a landfalling hurricane that produced a 300-year flood event over large portions of North and South Carolina, a 1000-year flood event in some areas (Griffin et al., 2019), 53 fatalities and more than $16 billion in property damage (Paul et al., 2019). Stored in the relatively common cfradial netCDF format, we have presented the steps taken to dealiaze radial velocity data and archive the raw dual-polarization moment data. In addition, the procedure used to produce nearly 26 hr of dual-Doppler analyses during Florence's landfall is detailed, and the analyses are made available for community use. This is the longest record of dual-Doppler wind retrievals during the landfall of a hurricane to be recorded to date.

The dual-polarization differential phase information can be used to perform attenuation correction (Gu et al., 2011; Testud et al., 2000), and the corrected reflectivity and other dual-polarimetric variables can be used to estimate rainfall (Bringi et al., 2011) produced by different components of the hurricane circulation. These rainfall estimates can then be fed into hydrological models to examine river flooding (Krajewski & Smith, 2002), which was extreme during Florence, and used to study erosion of roadways (Wang et al., 2019) and other infrastructure.

The wind retrievals can be used to study the dynamics of outer and inner core rainbands (c.f., Li & Wang, 2012) and eyewall structure (Marks et al., 2008), particularly the contraction of an eyewall (Li et al., 2019), which occurred while the eye was in the wind retrieval domain. Additionally, the study of vortex Rossby waves (Corbosiero et al., 2006; Guimond et al., 2020) in the inner core can be examined. The winds can also be used to validate numerical simulations of Hurricane Florence using actual observations as opposed to simulated observations (Nolan et al., 2013) or evaluating parametric wind models used to estimate oceanic waves during tropical cyclone conditions (Ruiz-Salcines et al., 2019).

The dual-Doppler analyses can also aid in the delineation of water versus wind impacts, which is paramount to the wind engineering and insurance communities (Baradaranshoraka et al., 2017). For example, following the procedures of Alford et al. (2019b) for Hurricane Harvey, a map of the maximum windspeeds at each grid cell retrieved in the dual-Doppler analyses over an ~26-hr period including landfall (Figure 7) indicated that the strongest winds (in excess of 75 m/s) were observed offshore in the north-eastern part of the eastern dual-Doppler lobe about 7 hr before landfall. This area of maximum windspeed

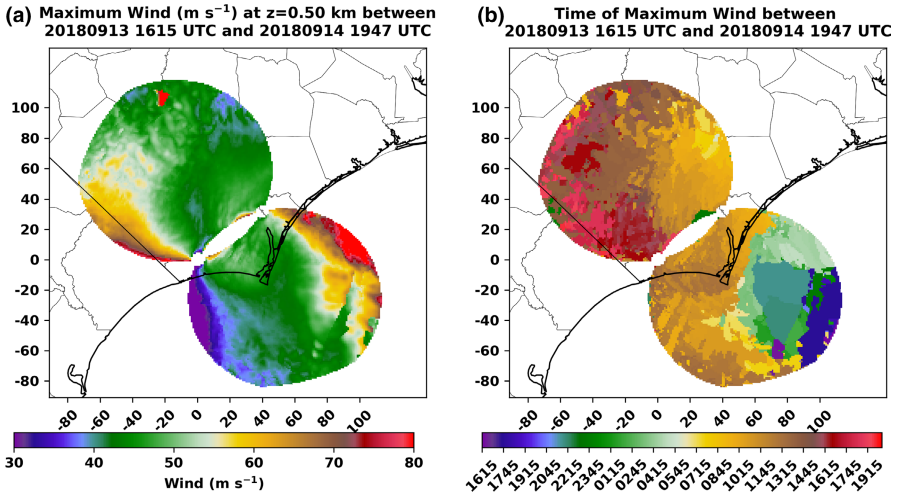

FIGURE 7 (a) Maximum wind speed at each 1 km by 1 km grid cell (in m/s) and (b) time of occurrence in UTC at 500 m altitude from the wind retrievals between 1616 UTC on 13 September and 1915 UTC on 14 September 2018 during the landfall of Hurricane Florence. The time labels correspond to the tick marks to the left

extended onshore within an hour of landfall to the northeast of Wrightsville Beach, NC where the centre of the eye of Florence crossed the coastline. No doubt extensive flooding associated with storm surge occurred in that area. The fastest winds over land are typically found along the coast in landfalling hurricanes (Alford et al., 2020). In Florence, a secondary region of windspeeds in excess of 70 m/s was observed about 20–40 km inland near the border of North and South Carolina over a sparsely populated region. This area of extreme winds occurred about 7 hr after landfall. Preliminary analysis of the evolution of the vortex (not shown) indicates that the onshore component of flow increased after landfall during the time period observed. In a future study, we will project these wind estimates to the surface to construct additional maps of wind characteristics associated with the landfall of Florence. We therefore anticipate uses of this dataset and similar future datasets beyond the meteorological community to achieve a more comprehensive, interdisciplinary assessment of TCs at landfall.

ACKNOWLEDGMENTS

Data collection for this study was supported by RAPID grant AGS-1902593 from the National Science Foundation, grant 70NANB19H056 from the National Institute for Standards and Technology and funds from the School of Meteorology at the University of Oklahoma. A. Alford was supported by NASA Headquarters under the NASA Earth and Space Science Fellowship Program grants 16-EARTH16F-0101, 17-EARTH17R-72 and 18-EARTH18R-0086 and the University of Oklahoma Nancy L. Mergler Dissertation Fellowship.

AUTHOR CONTRIBUTIONS

Michael I. Biggerstaff: Conceptualization (lead); Data curation (lead); Funding acquisition (lead); Investigation (lead); Methodology (equal); Project administration (lead); Resources (lead); Supervision (lead); Writing-original draft (lead); Writing-review & editing (lead). **A. Addison Alford:** Data curation (supporting); Formal analysis (lead); Investigation (supporting); Methodology (equal); Resources (supporting); Software (lead); Writing-original draft (supporting). **Gordon D. Carrie:** Data curation (supporting); Formal analysis (supporting); Project administration (supporting); Resources (supporting); Software (supporting); Writing-original draft (supporting). **Jeffrey A. Stevenson:** Data curation (supporting); Formal analysis (supporting); Investigation (supporting); Methodology (supporting).

OPEN PRACTICES

This article has earned an Open Data badge for making publicly available the digitally-shareable data necessary to reproduce the reported results. The data is available at https://doi.org/10.5281/zenodo.4594350. Learn more about the Open Practices badges from the Center for OpenScience: https://osf.io/tvyxz/wiki.

ORCID

Michael I. Biggerstaff https://orcid.org/0000-0002-6690-784X
A. Addison Alford https://orcid.org/0000-0001-7598-3783

REFERENCES

Alford, A.A., Biggerstaff, M.I. & Carrie, G.D. (2019a) Mobile ground-based SMART radar observations and wind retrievals during the landfall of Hurricane Harvey (2017). *Geoscience Data Journal*, 6, 205–213. Available from: https://doi.org/10.1002/gdj3.82

Alford, A.A., Biggerstaff, M.I., Carrie, G.D., Schroeder, J.L., Hirth, B.D. & Waugh, S.M. (2019b) Near-surface maximum winds during the landfall of Hurricane Harvey. *Geophysical Research Letters*, 46, 973–982. Available from: https://doi.org/10.1029/2018GL080013

Alford, A.A., Zhang, J.A., Biggerstaff, M.I., Dodge, P., Marks, F.D. & Bodine, D.J. (2020) Transition of the hurricane boundary layer during the landfall of Hurricane Irene (2011). *Journal of Atmospheric Science*, 77, 3509–3531. Available from: https://doi.org/10.1175/JAS-D-19-0290.1

Baradaranshoraka, M., Pinelli, J.-P., Gurley, K., Peng, X. & Zhao, M. (2017) Hurricane wind versus storm surge damage in the context of a risk prediction model. *Journal of the Structural Engineering. American Society of Civil Engineers*, 143, 1–10. Available from: https://doi.org/10.1061/(ASCE)ST.1943-541X.0001824

Barnes, S.L. (1994) Applications of the Barnes objective analysis scheme. Part III: Tuning for minimum error. *Journal of Atmospheric and Oceanic Technology*, 11, 1459–1479. Available from: https://doi.org/10.1175/1520-0426(1994)011<1459:AOTBOA>2.0.CO;2

Barth, M.C., Cantrell, C.A., Brune, W.H., Rutledge, S.A., Crawford, J.H., Huntrieser, H. et al. (2015) The Deep Convective Clouds and Chemistry (DC3) field campaign. *Bulletin of the American Meteorological Society*, 96, 1281–1309. Available from: https://doi.org/10.1175/BAMS-D-13-00290.1

Bela, M.M., Barth, M.C., Toon, O.B., Fried, A., Ziegler, C. & Cummings, K.A. et al. (2018) Effects of scavenging, entrainment, and aqueous chemistry on peroxides and formaldehyde in deep convective outflow over the central and Southeast U. S. *Journal of Geophysical Research: Atmospheres*, 123, 7594–7614. Available from: https://doi.org/10.1029/2018JD028271

Betten, D.P., Biggerstaff, M.I. & Ziegler, C.L. (2018) Three-dimensional storm structure and low-level boundaries at different stages of cyclic mesocyclone evolution in a high-precipitation tornadic supercell. *Advances in Meteorology*, 2018, 1–24. Available from: https://doi.org/10.1155/2018/9432670

Biggerstaff, M.I. & Houze, R.A., Jr. (1991) Kinematic and precipitation structure of the 10–11 June 1985 squall line. *Monthly Weather Review*, 119, 3034–3065. Available from: https://doi.org/10.1175/1520-0493(1991)119<3034:KAPSOT>2.0.CO;2

Biggerstaff, M.I., Wicker, L.J., Guynes, J., Ziegler, C., Straka, J.M., Rasmussen, E.N. et al. (2005) The Shared Mobile Atmospheric Research and Teaching (SMART) Radar: a collaboration to enhance research and teaching. *Bulletin of the American Meteorological Society*, 86, 1263–1274. Available from: https://doi.org/10.1175/BAMS-86-9-1263

Biggerstaff, M.I., Zounes, Z., Addison, A.A., Carrie, G.D., Pilkey, J.T., Uman, M.A. et al. (2017) Flash propagation and inferred charge structure relative to radar-observed ice alignment signatures in a small Florida Mesoscale Convective System. *Geophysical Research Letters*, 44, 8027–8036. Available from: https://doi.org/10.1002/2017GL074610

Bringi, V.N., Rico-Ramirez, M.A. & Thurai, M. (2011) Rainfall estimation with an operational polarimetric C-band radar in the United Kingdom: comparison with a gauge network and error analysis. *Journal of Hydrometeorology*, 12, 935–954. Available from: https://doi.org/10.1175/JHM-D-10-05013.1

Bruning, E.C., Rust, W.D., MacGorman, D.R., Biggerstaff, M.I. & Schuur, T. (2010) Formation of charge structures in a supercell. *Monthly Weather Review*, 138, 3740–3761. Available from: https://doi.org/10.1175/2010MWR3160.1

Calhoun, K.M., MacGorman, D.R., Ziegler, C.L. & Biggerstaff, M.I. (2013) Evolution of lightning activity and storm charge relative to dual-Doppler analysis of a high precipitation supercell storm. *Monthly Weather Review*, 141, 2199–2223. Available from: https://doi.org/10.1175/MWR-D-12-00258.1

Chmielewski, V.C., MacGorman, D.R., Ziegler, C.L., DiGangi, E., Betten, D. & Biggerstaff, M.I. (2020) Microphysical and transportive contributions to normal and anomalous polarity subregions in the 29–30 May 2012 Kingfisher storm. *Journal of Geophysical Research: Atmospheres*, 125, 29–30. Available from: https://doi.org/10.1029/2020JD032384

Chong, M., Testud, J. & Roux, F. (1983) Three-dimensional wind field analysis from Dual-Doppler Radar Data. Part II: minimizing the error due to temporal variation. *Journal of Applied Meteorology and Climatology*, 22, 1216–1226. Available from: https://doi.org/10.1175/1520-0450(1983)022<1216:TDWFAF>2.0.CO;2

Corbosiero, K.L., Molinari, J., Aiyyer, A.R. & Black, M.L. (2006) The structure and evolution of Hurricane Elena (1985). Part II: convective asymmetries and evidence for vortex rossby waves. *Monthly Weather Review*, 134, 3073–3091. Available from: https://doi.org/10.1175/MWR3250.1

Cressman, G.P. (1959) An operational objective analysis system. *Monthly Weather Review*, 87, 367–374. Available from: https://doi.org/10.1175/1520-0493(1959)087<0367:AOOAS>2.0.CO;2

Crum, T.D. & Alberty, R.L. (1993) The WSR-88D and the WSR-88D Operational Support Facility. *Bulletin of the American Meteorological Society*, 74, 1669–1687. Available from: https://doi.org/10.1175/1520-0477(1993)074<1669:TWATWO>2.0.CO;2

Davenport, C.E., Ziegler, C.L. & Biggerstaff, M.I. (2019) Creating a more realistic idealized supercell thunderstorm evolution via incorporation of base-state environmental variability. *Monthly Weather Review*, 147, 4177–4198. Available from: https://doi.org/10.1175/MWR-D-18-0447.1

DiGangi, E.A., MacGorman, D.R., Ziegler, C.L., Betten, D., Biggerstaff, M., Bowlan, M. et al. (2016) An overview of the 29 May 2012 kingfisher supercell during DC3. *Journal of Geophysical Research*, 121, 14316–14343. Available from: https://doi.org/10.1002/2016JD025690

Dixon, M. (2010) *Cf/Radial RADAR/LIDAR data format*. National Center for Atmospheric Research. Available from: https://ral.ucar.edu/projects/titan/docs/radial_formats/cfradial.html

Doviak, R.J., Bringi, V., Ryzhkov, A., Zahrai, A. & Zrnić, D. (2000) Considerations for polarimetric upgrades to operational WSR-88D radars. *Journal of Atmospheric and Oceanic Technology*, 17, 257–278. Available from: https://doi.org/10.1175/1520-0426(2000)017<0257:CFPUTO>2.0.CO;2

Doviak, R.J. & Zrnić, D.S. (1993) *Doppler radar and weather observations* (2nd ed., p. 42) Mineola, NY: Dover Publications.

Dowell, D.C. & Shapiro, A. (2003) Stability of an iterative dual-Doppler wind synthesis in Cartesian coordinates. *Journal of Atmospheric and Oceanic Technology*, 20, 1552–1559. Available from: https://doi.org/10.1175/1520-0426(2003)020<1552:SOAIDW>2.0.CO;2

Fernández-Cabán, P.L., Alford, A.A., Bell, M.J., Biggerstaff, M.I., Carrie, G.D., Hirth, B. et al. (2019) Observing Hurricane Harvey's eyewall at landfall. *Bulletin of the American Meteorological Society*, 100, 759–775. Available from: https://doi.org/10.1175/BAMS-D-17-0237.1

Foster, R.C. (2005) Why rolls are prevalent in the hurricane boundary layer. *Journal of Atmospheric Science*, 62, 2647–2661. Available from: https://doi.org/10.1175/JAS3475.1

Fried, A., Barth, M.C., Bela, M., Weibring, P., Richter, D., Walega, J. et al. (2016) Convective transport and scavenging of formaldehyde to the upper troposphere and lower stratosphere in thunderstorms over the Central United States During the 2012 DC3 Study. *Journal of Geophysical Research: Atmospheres*, 121, 7430–7460. Available from: https://doi.org/10.1002/2015JD024477

Geerts, B., Parsons, D., Ziegler, C., Weckwerth, T., Turner, D., Wurman, J. et al. (2017) The 2015 Plains Elevated Convection at Night (PECAN) field project. *Bulletin of the American Meteorological Society*, 98, 767–786. Available from: https://doi.org/10.1175/BAMS-D-15-00257.1

Griffin, M., Malsick, M., Mizzell, H. & Moore, L. (2019) Historic rainfall and record-breaking flooding from Hurricane Florence in the Pee Dee watershed. *The Journal of South Carolina Water Resources*, 6, 28–35. Available from: https://doi.org/10.34068/JSCWR.06.03

Gu, J.Y., Ryzhkov, A., Zhang, P., Neilley, P., Knight, M., Wolf, B. et al. (2011) Polarimetric attenuation correction in heavy rain at C band. *Journal of Applied Meteorology and Climatology*, 50, 39–58. Available from: https://doi.org/10.1175/2010JAMC2258.1

Guimond, S.R., Reasor, P.D., Heymsfield, G.M. & McLinden, M.M. (2020) The dynamics of vortex Rossby waves and secondary eyewall development in Hurricane Matthew (2016): new insights from radar measurements. *Journal of Atmospheric Science*, 77, 2349–2374. Available from: https://doi.org/10.1175/JAS-D-19-0284.1

Hare, B.M., Uman, M.A., Dwyer, J.R., Jordan, D.M., Biggerstaff, M.I., Caicedo, J.A. et al. (2016) Ground-level observation of a terrestrial gamma ray flash initiated by a triggered lightning. *Journal of Geophysical Research: Atmospheres*, 121, 6511–6533. Available from: https://doi.org/10.1002/2015JD024426

Helmus, J.J. & Collis, S.M. (2016) The Python ARM Radar Toolkit (Py-ART), a library for working with weather radar data in the Python Programming Language. *Journal of Open Research*

Software, 4, e25. Available from: https://doi.org/10.5334/jors.119

Hill, J.D., Pilkey, J., Uman, M.A., Jordan, D.M., Rison, W., Krehbiel, P.R. et al. (2013) Correlated lightning mapping array and radar observations of the initial stages of three sequentially triggered Florida lightning discharges. *Journal of Geophysical Research: Atmospheres*, 118, 8460–8481. Available from: https://doi.org/10.1002/jgrd.50660

Hirth, B.D., Schroeder, J.L., Weiss, C.C., Smith, D.A. & Biggerstaff, M.I. (2012) Research radar analyses of the internal boundary layer over Cape Canaveral, Florida, during the Landfall of Hurricane Frances (2004). *Weather Forecast*, 27, 1349–1372. Available from: https://doi.org/10.1175/WAF-D-12-00014.1

Huntrieser, H., Lichtenstern, M., Scheibe, M., Aufmhoff, H., Schlager, H., Pucik, T. et al. (2016) On the origin of pronounced O3 gradients in the thunderstorm outflow region during DC3. *Journal of Geophysical Research: Atmospheres*, 121, 6600–6637. Available from: https://doi.org/10.1002/2015JD024279

Jackson, R., Collis, S., Lang, T., Potvin, C. & Munson, T. (2020) PyDDA: a pythonic direct data assimilation framework for wind retrievals. *Journal of Open Research Software*, 8, 20. Available from: https://doi.org/10.5334/jors.264

James, C.N. & Houze, J. (2001) A real-time four-dimensional Doppler dealiasing scheme. *Journal of Atmospheric and Oceanic Technology*, 18, 1674–1683. Available from: https://doi.org/10.1175/1520-0426(2001)018<1674:ARTFDD>2.0.CO;2

Knupp, K.R., Walters, J. & Biggerstaff, M. (2006) Doppler profiler and radar observations of boundary layer variability during the landfall of Tropical Storm Gabrielle. *Journal of the Atmospheric Sciences*, 63, 234–251. Available from: https://doi.org/10.1175/JAS3608.1

Krajewski, W.F. & Smith, J.A. (2002) Radar hydrology: rainfall estimation. *Advances in Water Resources*, 25, 1387–1394. Available from: https://doi.org/10.1016/S0309-1708(02)00062-3

Kuhlman, K.M., MacGorman, D.R., Biggerstaff, M.I. & Krehbiel, P.R. (2009) Lightning initiation in the anvils of two supercell storms. *Geophysical Research Letters*, 36, L07802. https://doi.org/10.1029/2008GL036650

Leise, J.A. (1981) *A multi-dimensional, scale-telescoped filter and data extension package*. NOAA Tech. Memo ERL WPL-82, 24 pp.

Li, Q. & Wang, Y. (2012) A comparison of inner and outer spiral rainbands in a numerically simulated tropical cyclone. *Monthly Weather Review*, 140, 2782–2805. Available from: https://doi.org/10.1175/MWR-D-11-00237.1

Li, Y., Pickering, K.E., Allen, D., Barth, M.C., Bela, M.M., Cummings, K.A. et al. (2017) Evaluation of deep convective transport in storms of different scales during DC3 field campaign using WRF-Chem with lightning data assimilation. *Journal of Geophysical Research: Atmospheres*, 122, 7140–7163. Available from: https://doi.org/10.1002/2017JD026461

Li, Y., Wang, Y. & Lin, Y. (2019) Revisiting the dynamics of eyewall contraction of tropical cyclones. *Journal of Atmospheric Science*, 76, 3229–3245. Available from: https://doi.org/10.1175/JAS-D-19-0076.1

Lorsolo, S., Schroeder, J.L., Dodge, P. & Marks, F., Jr. (2008) An observational study of hurricane boundary layer SMA–scale coherent structures. *Monthly Weather Review*, 136, 2871–2893. Available from: https://doi.org/10.1175/2008MWR2273.1

Lund, N.R., MacGorman, D.R., Schuur, T.J., Biggerstaff, M.I. & Rust, W.D. (2009) Relationships between lightning location and polarimetric radar signatures in a small mesoscale convective system. *Monthly Weather Review*, 137, 4151–4170. Available from: https://doi.org/10.1175/2009MWR2860.1

MacGorman, D.R., Biggerstaff, M.I., Waugh, S., Pilkey, J.T., Uman, M.A., Jordan, D.M. et al. (2015) Coordinated lightning, balloon-borne electric field and radar observations of triggered lightning flashes in north Florida. *Geophysical Research Letters*, 42, 5635–5643. https://doi.org/10.1002/2015GL064203

MacGorman, D.R., Rust, W.D., Schuur, T.J., Biggerstaff, M.I., Straka, J.M., Ziegler, C.L. et al. (2008) TELEX: the thunderstorm electrification and lightning experiment. *Bulletin of the American Meteorological Society*, 89, 997–1013. Available from: https://doi.org/10.1175/2007BAMS2352.1

Marks, F.D., Black, P.G., Montgomery, M.T. & Burpee, R.W. (2008) Structure of the eye and eyewall of hurricane Hugo (1989). *Monthly Weather Review*, 136, 1237–1259. Available from: https://doi.org/10.1175/2007MWR2073.1

Matrosov, S.Y., Clark, K.A. & Kingsmill, D.E. (2007) A polarimetric approach to identify rain, melting-layer, and snow regions for applying corrections to vertical profiles of reflectivity. *Journal of Applied Meteorology*, 46, 154–166. Available from: https://doi.org/10.1175/JAM2508.1

Miller, R.L., Ziegler, C.L. & Biggerstaff, M.I. (2020) Seven-Doppler radar and in situ analysis of the 25–26 June 2015 Kansas MCS during PECAN. *Monthly Weather Review*, 148, 211–240. Available from: https://doi.org/10.1175/MWR-D-19-0151-1

Morrison, I., Businger, S., Marks, F., Dodge, P. & Businger, J.A. (2005) An observational case for the prevalence of roll vortices in the hurricane boundary layer. *Journal of Atmospheric Science*, 62, 2662–2673. Available from: https://doi.org/10.1175/JAS3508.1

Nolan, D.S., Atlas, R., Bhatia, K.T. & Bucci, L.R. (2013) Development and validation of a hurricane nature run using joint OSSE nature run and the WRF model. *Journal of Advances in Modeling Earth Systems*, 5, 382–405. Available from: https://doi.org/10.1002/jame.20031

Oye, R.C., Mueller, C. & Smith, S. (1995) *Software for radar translation, visualization, editing, and interpolation*. 27th Conference on Radar Meteorology, Vail, CO, Amer. Meteor. Soc., pp. 359–361.

Palucki, J.L., Biggerstaff, M.I., MacGorman, D.R. & Schuur, T. (2011) Comparison between low-flash and non-lightning producing convection in a mature mesoscale convective system. *Weather and Forecasting*, 26, 468–486. Available from: https://doi.org/10.1175/WAF-D-10-05012.1

Paul, S., Ghebreyesus, D. & Sharif, H. (2019) Brief communication: Analysis of the fatalities and socio-economic impacts caused by Hurricane Florence. *Geoscience*, 9, 1–12. Available from: https://doi.org/10.3390/geosciences9020058

Payne, C.D., Schuur, T.J., MacGorman, D.R., Biggerstaff, M.I., Kuhlman, K. & Rust, W.D. (2010) Polarimetric and electrical characteristics of a lightning ring in a supercell storm. *Monthly Weather Review*, 138, 2405–2425. Available from: https://doi.org/10.1175/2009MWR3210.1

Pilkey, J., Uman, M.A., Hill, J.D., Ngin, T., Gamerota, W., Jordan, D. et al. (2013) Rocket-and-wire triggered lightning in 2012 Tropical Storm Debby in the absence of natural lightning. *Journal of Geophysical Research: Atmospheres*, 118, 13158–13174. Available from: https://doi.org/10.1002/2013JD020501

Potvin, C.K., Betten, D., Wicker, L.J., Elmore, K.L. & Biggerstaff, M.I. (2012a) 3DVAR vs. traditional dual-Doppler wind retrievals of a simulated supercell thunderstorm. *Monthly Weather Review*, 140, 3487–3494. Available from: https://doi.org/10.1175/MWR-D-12-00063.1

Potvin, C.K., Wicker, L.J. & Shapiro, A. (2012b) Assessing errors in variational Dual-Doppler wind syntheses of supercell thunderstorms observed by storm-scale mobile radars. *Journal of Atmospheric and Oceanic Technology*, 29, 1009–1025. Available from: https://doi.org/10.1175/JTECH-D-11-00177.1

Rew, R., David, G., Emmerson, S., Davies, H., Hartnett, E., Heimbigner, D. et al. (2018) *NetCDF overview*. Available from: https://www.unidata.ucar.edu/software/netcdf/docs/

Ruiz-Salcines, P., Salles, P., Robles-Diaz, L., Diaz-Hernandez, G., Torres-Freyermuth, A. & Appendini, C.M. (2019) On the use of parametric wind models for wind wave modeling under tropical cyclones. *Water*, 11, 1–23. Available from: https://doi.org/10.3990/w11102044

Ryzhkov, A.V., Schuur, T.J., Burgess, D.W. & Zrnic, D.S. (2005) Polarimetric Tornado detection. *Journal of Applied Meteorology*, 44, 557–570. Available from: https://doi.org/10.1175/JAM2235.1

Shapiro, A., Gebauer, J.G., Dahl, N.A., Bodine, D.J., Mahre, A. & Potvin, C.K. (2021) Spatially variable advection correction of Doppler radial velocity data. *Journal of Atmospheric Science*, 78, 167–188. Available from: https://doi.org/10.1175/JAS-D-20-0048.1

Shapiro, A., Willingham, K.M. & Potvin, C.K. (2010) Spatially variable advection correction of radar data. Part I: Theoretical considerations. *Journal of Atmospheric Science*, 67, 3445–3456. Available from: https://doi.org/10.1175/2010JAS3465.1

Sibson, R. (1981) A brief description of natural neighbor interpolation. In: Barnett, V. (Ed.) *Interpreting multivariate data*. New York, NY: John Wiley & Sons, pp. 21–36.

Skinner, P.S., Weiss, C.C., Schroeder, J.L., Wicker, L.J. & Biggerstaff, M.I. (2011) Observations of the surface boundary structure within the 23 May 2007 Perryton, Texas supercell. *Monthly Weather Review*, 139, 3730–3749. Available from: https://doi.org/10.1175/MWR-D-10-05078.1

Stepanian, P.M., Horton, K.G., Melnikov, V.M., Zrnić, D.S. & Gauthreaux, S.A. (2016) Dual-polarization radar products for biological applications. *Ecosphere*, 7, 1–27. Available from: https://doi.org/10.1002/ecs2.1539

Stewart, S.R. & Berg, R. (2019) *National Hurricane Center Tropical Cyclone Report: Hurricane Florence (AL062018)*. Available from: https://www.nhc.noaa.gov/data/tcr/AL062018_Florence.pdf

Testud, J., Le Bouar, E., Obligis, E. & Ali-Mehenni, M. (2000) The rain profiling algorithm applied to polarimertic weather radar. *Journal of Atmospheric and Oceanic Technology*, 17, 332–356. Available from: https://doi.org/10.1175/1520-0426(2000)017<0332:TRPAAT>2.0.CO;2

Vaisala (2014) *RVP8 user's manual* (p. 525). Available from: ftp://ftp.sigmet.com/outgoing/manuals/RVP8_Users_Manual.pdf

Wang, W., Yang, S., Stanley, H.E. & Gao, J. (2019) Local floods induce large-scale abrupt failures of road networks. *Nature Communications*, 10, 1–11. Available from: https://doi.org/10.1038/s41467-019-10063-w

Ziegler, C.L. (2013) A diabatic Lagrangian technique for the analysis of convective storms. Part II: Application to a radar-observed storm. *Journal of Atmospheric and Oceanic Technology*, 30, 2266–2280. Available from: https://doi.org/10.1175/JTECH-D-13-00036.1

Zittel, W.D., Saxion, D., Rhoton, R. & Crauder, D. (2008) *Combined WSR-88D technique to reduce range aliasing using phase coding and multiple Doppler scans*. 24th International Conf. on Interactive Information and Processing Systems for Meteorology, Oceanography, and Hydrology, New Orleans, LA, Amer. Meteor. Soc.

Zrnić, D.S., Keenan, T.D., Carey, L.D. & May, P. (2000) Sensitivity analysis of polarimetric variables at a 5-cm wavelength in rain. *Journal of Applied Meteorology*, 39, 1514–1526. Available from: https://doi.org/10.1175/1520-0450(2000)039<1514:SAOPVA>2.0.CO;2

How to cite this article: Biggerstaff, M.I., Alford, A.A., Carrie, G.D. & Stevenson, J.A. (2022) Hurricane Florence (2018): Long duration single- and dual-Doppler observations and wind retrievals during landfall. *Geoscience Data Journal*, 9, 273–287. https://doi.org/10.1002/gdj3.137